

## CFD Validation of Shock-Shock Interaction Flow Fields

**S. Walker\* and J.D. Schmisser†**  
Air Force Office of Scientific Research  
Air Force Research Laboratory  
Arlington, VA 22203-1977  
USA

### ABSTRACT

*Current capabilities for numerical simulation of laminar shock-shock interactions are examined. Two fundamental configurations are considered: the Edney IV shock-shock interaction and the crossing oblique-shock interaction generated by a double wedge configuration. Two cases for each configuration were examined by a distinguished group of international researchers using the Reynolds-averaged Navier-Stokes (RANS) equations and Direct Simulation Monte Carlo (DSMC) methods. The report presents an extensive comparison of the submitted computations and experimental data.*

### INTRODUCTION

Accurate prediction of the flow field resulting from the interaction of shock waves is critical for the design of efficient air-breathing hypersonic vehicles. In an effort to advance hypersonic- vehicle related technologies the NATO Research Technology Organization (RTO) Advanced Vehicle Technology Panel Working Group 10 (WG 10) has examined the current state-of-the-art in numerical simulations. The following report summarizes the work of the CFD validation subgroup of WG 10 in the area of validation of numerically simulated laminar shock-shock interactions.

Two geometrically simple, yet computationally challenging, flow fields were chosen for this study. The first is the well-known Edney type IV interaction [1] that can result in extreme pressure and heat loads. The second is the flow field resulting from crossing oblique shocks generated by opposing wedges. While on the surface this interaction appears rather simple, in the *dual-solution* domain, [2] between the theoretical Neumann and detachment conditions, both regular and irregular reflections are possible and hysteresis in the reflection configuration has been observed.

Two test cases for each of the interactions described above were characterized experimentally and numerically simulated during the course of the WG 10 effort. The remainder of this manuscript describes the results for first the Edney IV interaction and then the crossing oblique-shock interaction.

### EDNEY IV SHOCK-SHOCK INTERACTION

The heating rates generated by shock-shock interactions can result in some of the most severe heating loads imposed on the thermal protection systems of hypersonic lifting bodies and air-breathing propulsion systems. In regions near a leading edge heating levels up to 30 times those encountered in an undisturbed stagnation

---

\* Program Manager, Currently Special Assistant DDR&E, Assoc. Fellow AIAA.

† Program Manager, Senior Member AIAA.

Report Documentation Page				Form Approved OMB No. 0704-0188	
Public reporting burden for the collection of information is estimated to average 1 hour per response, including the time for reviewing instructions, searching existing data sources, gathering and maintaining the data needed, and completing and reviewing the collection of information. Send comments regarding this burden estimate or any other aspect of this collection of information, including suggestions for reducing this burden, to Washington Headquarters Services, Directorate for Information Operations and Reports, 1215 Jefferson Davis Highway, Suite 1204, Arlington VA 22202-4302. Respondents should be aware that notwithstanding any other provision of law, no person shall be subject to a penalty for failing to comply with a collection of information if it does not display a currently valid OMB control number.					
1. REPORT DATE <b>01 JAN 2006</b>		2. REPORT TYPE <b>N/A</b>		3. DATES COVERED <b>-</b>	
4. TITLE AND SUBTITLE <b>CFD Validation of Shock-Shock Interaction Flow Fields</b>				5a. CONTRACT NUMBER	
				5b. GRANT NUMBER	
				5c. PROGRAM ELEMENT NUMBER	
6. AUTHOR(S)				5d. PROJECT NUMBER	
				5e. TASK NUMBER	
				5f. WORK UNIT NUMBER	
7. PERFORMING ORGANIZATION NAME(S) AND ADDRESS(ES) <b>Air Force Office of Scientific Research Air Force Research Laboratory Arlington, VA 22203-1977 USA</b>				8. PERFORMING ORGANIZATION REPORT NUMBER	
9. SPONSORING/MONITORING AGENCY NAME(S) AND ADDRESS(ES)				10. SPONSOR/MONITOR'S ACRONYM(S)	
				11. SPONSOR/MONITOR'S REPORT NUMBER(S)	
12. DISTRIBUTION/AVAILABILITY STATEMENT <b>Approved for public release, distribution unlimited</b>					
13. SUPPLEMENTARY NOTES <b>See also ADM001860, Technologies for Propelled Hypersonic Flight (Technologies des vols hypersoniques propulsés). , The original document contains color images.</b>					
14. ABSTRACT					
15. SUBJECT TERMS					
16. SECURITY CLASSIFICATION OF:			17. LIMITATION OF ABSTRACT <b>UU</b>	18. NUMBER OF PAGES <b>26</b>	19a. NAME OF RESPONSIBLE PERSON
a. REPORT <b>unclassified</b>	b. ABSTRACT <b>unclassified</b>	c. THIS PAGE <b>unclassified</b>			

flow can be generated. In these regions the strong gradients, unsteadiness and transitional nature of the flow combine to make accurate prediction of the flow field a challenging endeavor.

The severe heating loads developed in a shock-shock interaction were first studied in detail following the X-15 scramjet program where shock-shock heating resulted in a structural failure in the pylon supporting the scramjet engine [3]. A series of studies were conducted in the late 1960s where the main focus was the interaction between a shock wave and vertical fin. The studies by Edney [1] of shock interactions on spherical configurations, coupled with his analysis of various interaction geometries that can be developed over cylinders and struts, provided the basic groundwork for the semi-empirical prediction of these flows. A review of these earlier studies together with measurements of heat transfer and pressure distribution in regions of shock-shock interaction over cylindrical leading edges in laminar, transitional and turbulent interaction regions were presented by Holden et al [4].

Historically, the empirical modeling of these flows has been based on defining a small stagnation region downstream of a jet like flow such as that observed in the Type IV interaction [1] (Fig. 1). However, experiments have revealed that it is extremely difficult to distinguish between the heating loads generated by the various flow field elements such as the strong viscous effects or transitional nature of the shear layer. It has been observed that the heating rates derived from an Edney IV shock-shock interaction vary widely depending on whether the flow is laminar, transitional or turbulent as well as whether the gas is considered perfect or real. In laminar flow, both Navier-Stokes and DSMC predictions have compared well with experiments if well-defined grid resolution studies are performed. When the shear layers or the boundary layers in the reattachment region become transitional a significant increase in the heating load results.

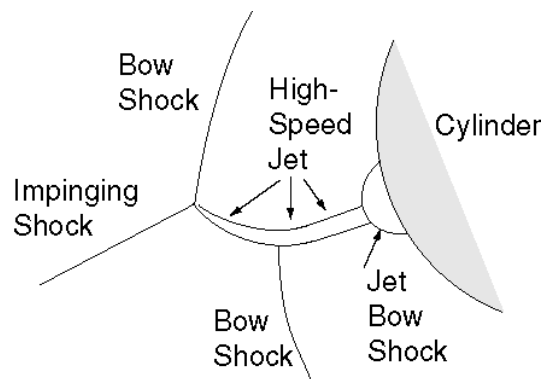


**Figure 1: Schematic of Edney Type IV Shock-Shock Interaction.**

Edney also demonstrated that the jet like model proposed for the Type IV interaction was highly sensitive to the specific heat ratio and the freestream Mach number through the sensitivity of the compression processes to these parameters. Specifically, he concluded that real gas effects could lower specific heat ratio, and result in significant increases in heating in these regions. Experimental studies of this have yielded conflicting results and computational techniques, both Navier-Stokes and DSMC, have shown 50% increases in peak heating rates over ideal gas heating predictions [5].

In summary, the Edney IV shock-shock interaction flow field is a complex shock-shock interaction relevant to high-speed airframe-propulsion integration designs. Given the geometric simplicity of the shock generators and the numerical challenges associated with accurate simulation of the resulting flow field, it is an excellent test case for CFD validation studies for propelled vehicles in hypersonic flight.

## ONERA TEST CASE

The first test case considered for validation of simulated Edney IV shock-shock interactions is an experiment conducted in the R5Ch test facility of ONERA headed by Prof. J. D'elery, France [6].

### Description of Experiment

The arrangement of the cylinder and the wedge models in the test section is shown in Figure 2. The relative locations of the cylinder and the wedge are selected in order to obtain a Type IV shock-shock interaction. The wedge angle is  $20^\circ$  and the wedge length is equal to  $L = 0.1$  m. Its span is 0.1 m. The axis of the cylinder is perpendicular to the free stream direction. The distance between the leading edge of the shock generator and the cylinder center is 0.110 m along the x-axis (streamwise direction) and 0.053 m along y-axis (perpendicular to the upstream flow direction). The origin of the coordinate system for all of the data comparisons presented is located at the stagnation point of the cylinder. The mesh coordinates are non-dimensionalized by the cylinder radius  $R = 0.008$  m.

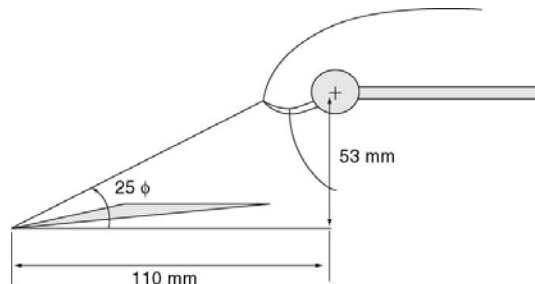


Figure 2: Schematic of Edney IV Shock-Shock Interaction Generator.

The important flow parameters are as follows: Perfect gas  $\gamma = 1.4$ , two-dimensional, fully laminar flow, and laminar viscosity ( $3.405 \times 10^{-6}$  Pa.s) by Sutherland's Law.

The cylinder is equipped with thermocouples and pressure taps. The experimental data includes wall pressure, wall heat flux, flow field visualization by the Electron Beam Fluorescence technique, and density and temperature measurement in the flow field interaction (more than 100 data points).

The nominal stagnation conditions are  $P_o = 2.5$  bars and  $T = 1050$  K which yield the freestream properties of  $M_{oo} = 10$ ,  $T_{oo} = 52.5$  K,  $P_{oo} = 5.9$  Pa, and  $Re_{oo}/m = 1.66 \times 10^5$ . The Reynolds number, based on the cylinder diameter (0.016 m) is 2658.

### Computational Contributions

The three contributors to this test case were Dr. James Moss, NASA Langley Research Center, Hampton, VA, Dr. Domenic D'Ambrosio, Politecnico di Torino, Torino, Italy and Dr. Marco Marini, CIRA, Capua, Italy.

Moss used the general 2D/axisymmetric DSMC code of Bird [7], in which the molecular collisions are simulated by using the variable hard sphere (VHS) molecular model. These simulations utilized a nonreacting gas model consisting of two species while considering energy exchange between translational, rotational, and vibrational modes. The calculations were made following a grid resolution and time step sensitivity study.

## CFD Validation of Shock-Shock Interaction Flow Fields

---

Three different grids were used whereby the overall computational domain was subdivided into 13 arbitrary regions. The number of cells/subcells used for the three grids were as follows:

coarsest – 29,200/116,800;

intermediate – 63,510/254,040; and

finest – 97,060/958,490.

The computational time step was reduced as the grids were refined. For more detailed information on the DSMC calculation procedure used, see Moss, et al. [8]

D'Ambrosio's numerical technique employs a finite volume method over structured grids and is based on a flux-difference splitting scheme for evaluating convective fluxes at volume surfaces. Second order accuracy in space and in time is achieved by means of ENO-like linear interpolation of Riemann invariants in the whole flow field. Diffusive fluxes are computed through centered differences, which are inherently second order accurate. Numerical results were obtained using a grid composed of 300 x 351 points in the radial and tangential directions respectively. Grid points were clustered close to the wall in the radial direction and in the region where the interaction occurs in the tangential direction. A preliminary numerical investigation has shown a noticeable sensitivity of the interaction pattern to the impinging shock position. For this reason, in order to reproduce the experiments correctly, inflow conditions for the computation were defined by interpolating numerical results obtained considering the real shock generator configuration. The final results appear to be steady. Convergence of the solutions was tested by recording pressure time histories at four different flow field locations.

Marini used the CIRA H2NS (Hypersonic 2D Navier-Stokes) code which uses a finite volume technique over a structured mesh, with fluxes at the interfaces computed using a Flux Difference Splitting Riemann Solver with a second order reconstruction of the interface values. The viscous fluxes are calculated by central differencing, and time integration is performed by employing an explicit multistage Runge-Kutta algorithm with optimized coefficients coupled with an implicit evaluation of the source terms. The sensitivity to grid refinement and to different boundary conditions that simulate the flow entering the computational domain was investigated. Two different computational grids were employed: a coarse grid (180X90) and a fine grid (270X136). The grid points were clustered in both logical directions around the stagnation point. The steadiness of jet impingement angular location over the cylinder and the peak values of pressure and heat transfer are assumed as convergence criteria rather than the classical root mean square of the density equation residual.

### Computational Results

The static pressure and heat transfer comparisons on the cylinder are shown in Fig. 3a-b. In general, the computational peak pressure and heat transfer are higher than the experimentally measured values. Part of the difference is due to the pressure measurement holes being large, 1.5 mm in diameter. One solution for making the computational and experimental comparisons more accurate was to average the numerical results over the pressure hole dimension. D'Ambrosio averaged his numerical results around the measurement location considering the 1.5 mm diameter of the pressure tap (data was averaged over a  $\pm 5.37$  degrees with respect to the center of the nominal measurement hole). The weighted average was based on the tangential stretching of the mesh. Comparing the averaged computations to the experimental measurements at the peak pressure location results in a very good match.

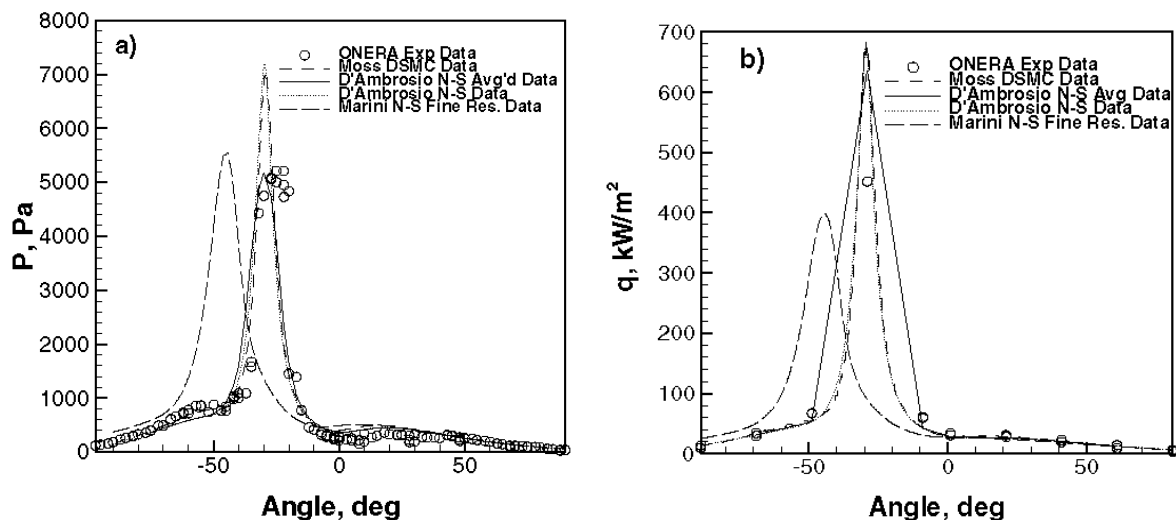
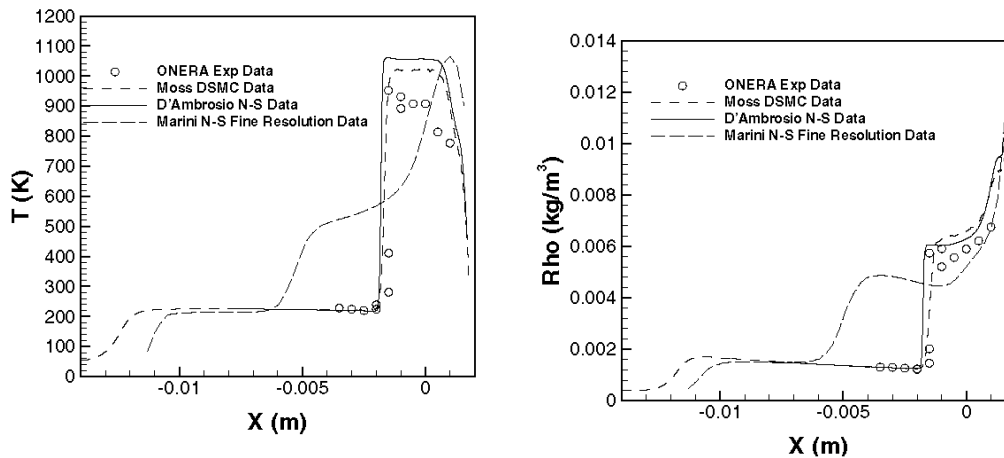


Figure 3: Comparison of Experimental and Computed Data for the ONERA Test Case.

In the case of the heat transfer, the thermocouple diameters are smaller, 0.4 mm and the difference between the original and averaged numerical data is smaller. However, there are too few experimental data points to determine whether the largest experimental value is the peak or just a point in the increasing or decreasing slopes around the peak.

The Marini fine resolution computations did not agree very well with the experimental data. Upon further investigation, it was discovered that Marini calculated the shock generator flow field separately from the cylinder flow field and input the former as an initial condition to the later. The problem with this approach is that the jet bow shock impingement is strongly dependent on the angle and strength of shock wave approaching the cylinder. The discrepancies between present computations and experiments are ascribed to the lack of the effects induced on the flow approaching the cylinder by the base flow occurring in the rear part of the shock generator.

Computational results along a horizontal line at  $Y=-0.005$  mm (below the shock impingement location) are compared to experimental temperature and density measurements in Figure 4a-b. Both the Moss and D'Ambrosio solutions do a fairly good job in predicting the temperature and density variation along the axial direction in this flow field, although both quantities are over predicted slightly. Again, the Marini data does not compare well probably due to the separate calculation of shock generator and cylinder flow fields.



**Figure 4: Comparison of Numerical and Experimental Results Along a Horizontal Line,  $Y = -0.005$  mm.**

In the simulations of the ONERA Edney IV shock-shock interaction, there seems to be a consistent over-prediction of the physical flow quantities when compared to the experimental results. This may be due to an observed unsteadiness in the experimental measurements. This unsteadiness could be inherent in the facility or due to the transitional jet shear layer instability in the flow. Given the observed unsteadiness, the discrepancy between the steady CFD results and the unsteady experimental measurements for the peak pressure and heat transfer location is not surprising.

## CUBRC TEST CASE

Holden [9] at the Calspan-University of Buffalo Research Center (CUBRC) developed the second Edney IV shock-shock interaction test case. Flow conditions, experimental setup, and detailed measurements are reported in Ref. 10.

### Description of Experiment

CUBRC conducted an extensive series of studies over a range of Mach numbers from 10 to 16 to define the aerothermal loads generated in regions of shock-shock interaction from the rarefied to the fully continuum turbulent flow regimes. Detailed heat transfer and pressure measurements were made in the 48-inch, 96-inch and LENS shock tunnels. The results of these studies were analyzed to provide guidance to predict the heating enhancement factors in laminar, transitional, and turbulent flows. The experimental data presented in this section are for fully laminar flows.

The CUBRC model configuration is shown in Figure 5. The regions of shock-shock interaction studied were generated over a series of cylindrical leading edge configurations with nose radii of 0.351, 0.953, and 3.81 cm. Each of these leading edges was densely instrumented with heat transfer instrumentation placed to have a circumferential resolution less than 1 degree. The thin-film instrumentation was deposited on a low-conductivity surface to minimize measurement errors associated with lateral conduction in the large heat transfer gradients generated in the region of peak heating. The high-frequency response of the thin-film instrumentation was also a key factor in accurately determining the heating distribution for shock-shock interactions, which exhibited intrinsic flow unsteadiness.

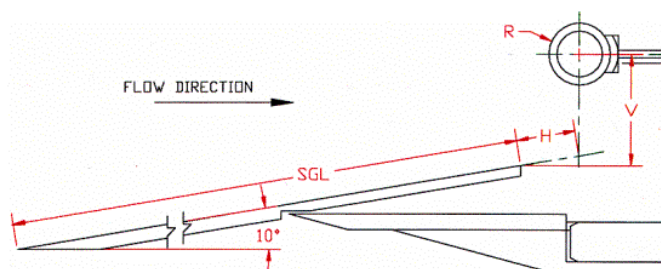


**Figure 5: Schematic of the CUBRC Edney IV Interaction Generator.**

The flow conditions for this study produced perfect gas, planar flow field, laminar flow shock-shock interactions. For the exact flow conditions of test runs 38, 43, 44, and 105, please see Table 1. The experimental data includes surface temperature, heat transfer, pressure distributions and Schlieren photographs.

**Table 1: CUBRC Test Conditions (V, H, SGL, R in inches)**

Run	Mach No.	Reynolds No.	V	H	SGL	R
38	14.15	1.587 E+4	4 1/16	-1 1/32	46 1/2	1.5
43	13.94	1.299 E+4	4 25/64	1 1/32	46 1/2	1.5
44	13.97	1.333 E+4	4 34/64	31/32	46 1/2	1.5
105	15.70	2.708 E+4	2 39/64	1 15/32	26 1/2	0.75

## Computational Contributions

The three contributors for this test case were Dr Domenic D'Ambrosio, Politecnico di Torino, Torino, Italy, Dr Graham Candler, University of Minnesota, Minneapolis, MN, and Dr. Iain Boyd, University of Michigan, Ann Arbor, MI.

D'Ambrosio's numerical technique was the same as that described above for the ONERA test case. Results were obtained using a coarse (75X150) and a fine (250X300) grid.

Candler's computations were performed with a CFD code that uses second-order accurate modified Steger-Warming flux vector splitting [11] and an implicit parallel time integration method [13]. The grid consisted of 382 points in the circumferential direction, and 256 points normal to the cylinder surface. The grid was exponentially stretched from the surface, and care was taken to have sufficient near-wall resolution to capture the large flow gradients at the surface. Because of the relatively low enthalpy conditions of the experiments, chemical reactions were not considered, however vibrational relaxation of the gas was allowed. A vibrational equilibrium free-stream was assumed. Standard transport property models were used for the gas as in Candler and MacCormack [12].

Candler computed post-shock conditions using the experimental free-stream conditions and the 10 deg. turning angle of the shock generator. The post-shock conditions were then used as inflow conditions everywhere below a specified distance from the cylinder centerline. This distance was adjusted until the maxima in the heat transfer rate and surface pressure were located at the same point on the cylinder as in the



experiments. This approach was required since very slight differences in the location of the shock generator relative to the cylinder result in large differences in the structure of the shock interaction.

The DSMC solutions provided by Boyd were performed using the MONACO code: a general, object-oriented, cell-based, parallelized implementation of the DSMC method developed by Dietrich and Boyd [14]. MONACO employs the Variable Soft Sphere (VSS) collision model of Koura et al [15], a variable rotational energy exchange probability model of Boyd [16] and the variable vibrational energy exchange probability model of Vijayakumar et al [17]. The flow conditions here do not involve chemical reactions. Simulations of particle/wall interaction employ accommodation and momentum reflection coefficients of 0.85. The present simulations employ grids of 512 by 512 cells (Run 105) and 1024 by 1024 cells (Run 43), which give maximum sizes of 2 local mean free paths. The time step employed in both simulations is  $(10)^{-9}$  sec and this is less than the local mean time between collisions everywhere. The total numbers of particles employed is 2 million (Run 105) and 8 million (Run 43). This allows the minimum number of particles per cell to be everywhere greater than 4. The simulations are performed on an IBM-SP computer at the University of Minnesota Supercomputing Institute using 4 processors (Run 105) and 16 processors (Run 43).

## Computational Results

A comparison of the numerical results with the measured CUBRC Run 38 data of Holden is shown in Figure 6(a,b). Both surface pressure and surface nondimensional heat transfer are plotted in angular coordinates around the cylinder. Inspection reveals that both the calculated pressure coefficient and heat transfer ratio are severely over-predicted. In a similar manner as described above, D'Ambrosio corrected this over-prediction by averaging his CFD results over the experimental measurement resolution. However, for the CUBRC experiments, this resolution was undetermined at the time of the computations. If similar averaging schemes were utilized, improved agreement between simulation and experiment resulting from the CFD-averaging process would suggest that the experiment is highly unsteady and that the data are actually average quantities of an unsteady, oscillating impinging jet.

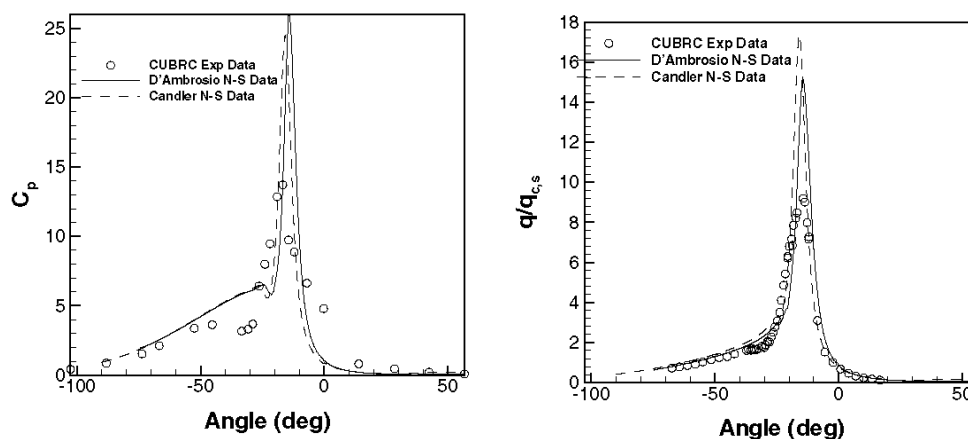


**Figure 6: Experimental and Numerical Results for the Conditions of CUBRC Run #38.**

D'Ambrosio and Candler produce slight different peak pressure and heat transfer locations on the cylinder. Both investigators attempted to match their peak data location with that of the experiment. These results show

that this is not a simple thing to do. Even if both investigators had determined the exact same peak pressure heat transfer location on the cylinder, this is clearly a post-dictive exercise, using the experimental data to determine the simulation results.

Run 38 is also interesting from the standpoint that surface pressures under the shock impingement location are poorly predicted by both investigators. Both investigators used the same shock intensity and inclination inflow conditions instead of calculating the shock generator flow field directly. This may be the root cause of the disagreement.

The pressure coefficient and heat transfer ratio comparisons for Runs 43, 44, and 105 are shown in Figures 7(a,b), 8(a,b), and 9(a,b). For these runs, the CUBRC experiments were simulated using Candler's Navier-Stokes and Boyd's DSMC methods. As with the earlier data, the peak pressure coefficient and heat transfer are over-predicted by the Navier-Stokes and DSMC methods. Again, there may be several reasons for the disagreement between the peak experimental data and the simulations.

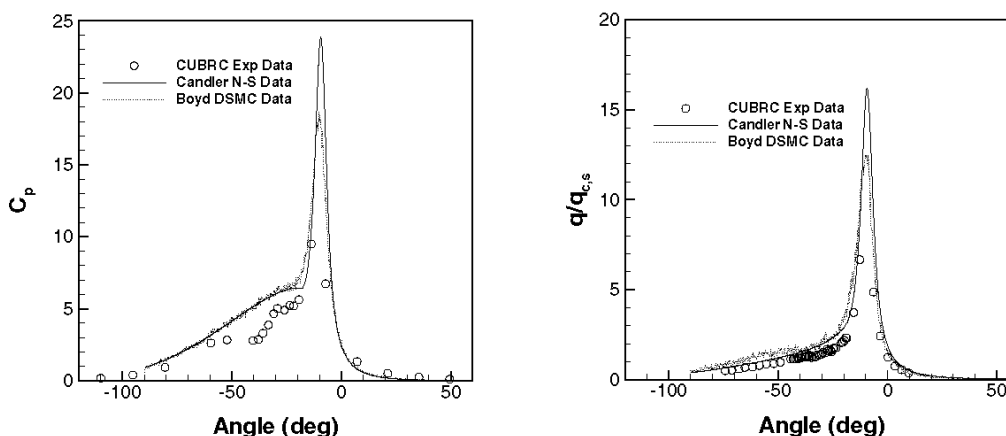


Figure 7: Experimental and Numerical Results for the Conditions of CUBRC Run #43.

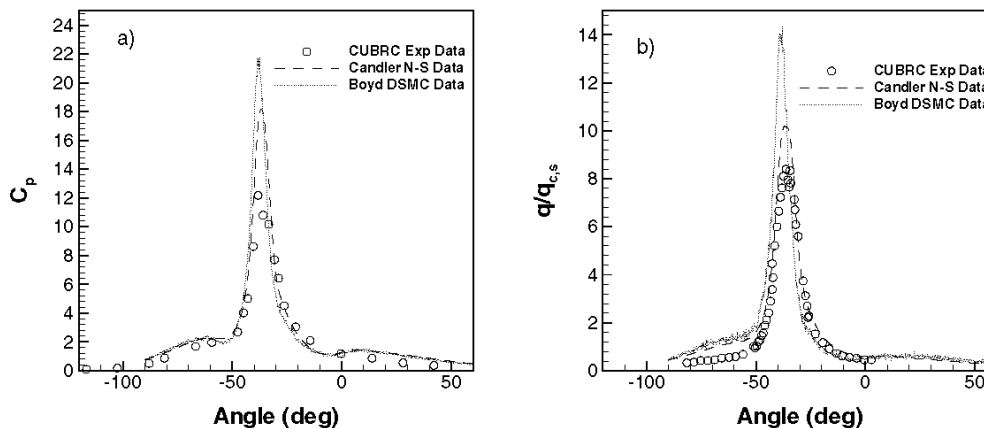
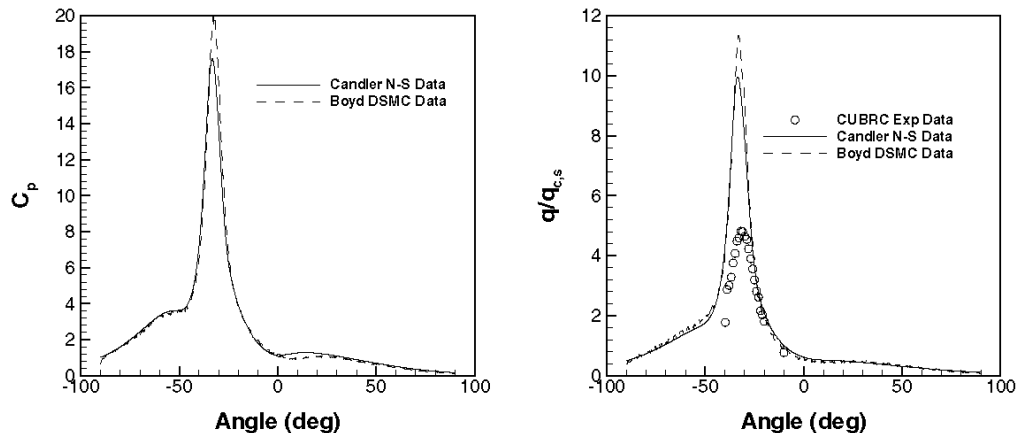


Figure 8: Experimental and Numerical Results for the Conditions of CUBRC Run #44.



**Figure 9: Experimental and Numerical Results for the Conditions of CUBRC Run #105.**

The sensitivity of the solutions to the shock impingement location may have an important effect on the interpretation of the experimental data. Slight variations in the free-stream conditions result in changes in the shock impingement location, which substantially change the surface quantities. Thus, it is possible that the experimental results represent some averaging of the shock impingement location. This would tend to broaden the peaks and reduce their magnitudes, as seen in the comparison between the computations and experiments. Another reason may be that because the cylinders are small in diameter, and the pressure instrumentation is limited, there are some cases where the actual peak pressure falls between two transducers and is not fully recorded. This may be the case, especially with Run 43, where there is almost no experimental peak pressure coefficient. (In Run 105, the cylinder was too small to incorporate any pressure sensors, so there is no experimental pressure data available for this case.)

The off-peak surface pressure coefficient beneath the interaction location is not well predicted by either Navier-Stokes or DSMC for Run 43, while the heat transfer ratio comparisons are much better. The good off-peak heat transfer comparisons may be a function of the better resolution of heat transfer instrumentation. Also, both Navier-Stokes and DSMC methods required several milliseconds to reach steady-state solutions and for some shock impingement locations, the solutions never did stabilize. Run 43 is a particularly strong interaction, and the supersonic jet impinging on the surface is likely to be unstable. Of course, the capacity for the present CFD simulations to accurately capture this unsteadiness is suspect.

Figure 8(a,b) shows the pressure coefficient and heat transfer for CUBRC Run 44. In this case, the off-peak pressure coefficients are well predicted by Navier-Stokes and DSMC, however the peak comparison is still not good. For heat transfer, the peak comparison is much better, especially for the Navier-Stokes, however the off-peak comparison beneath the impingement location is wrong. The translational temperature contours for both Navier-Stokes and DSMC are shown in Figure 10(a,b). Both methods predict similar flow fields. Overall, considering both peak and off-peak regions, Run 44 represents the best that DSMC and Navier-Stokes methods can offer. However, it is still apparent that there are many inconsistencies between the computational methods and the experimental data that need to be resolved.

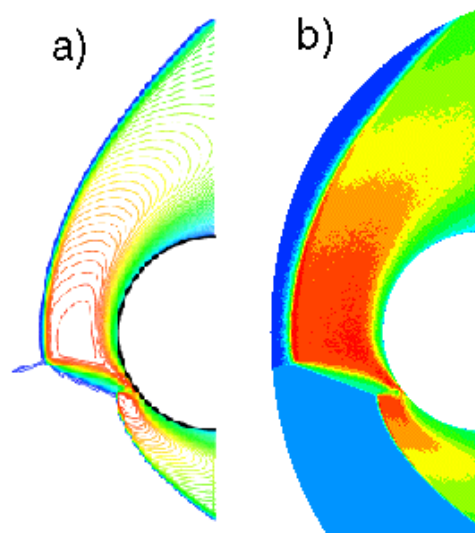
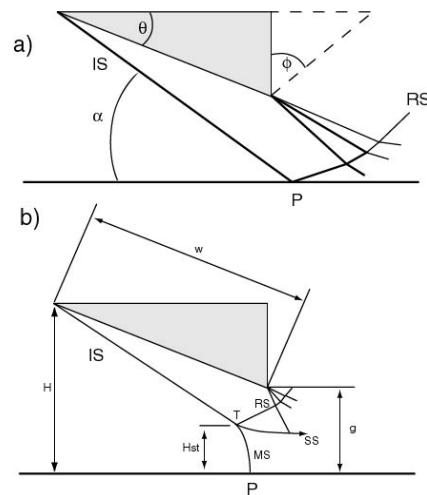


Figure 10: Contours of Constant Translational Temperature for a) Navier-Stokes and b) DSMC Solutions for the conditions of CUBRC Run #44.

## OBLIQUE CROSSING SHOCK INTERACTION

The structure and effects of shock waves in both internal and external flow fields influence supersonic/hypersonic vehicle operation. In general, shock waves interact with each other and with boundary layers developing on adjacent walls. The consequences include boundary layer separation and flow field distortion, which can significantly impact engine design and performance [18]. An important class of interactions is that comprised of crossing oblique shock waves that result in either regular or Mach (irregular) reflections.

For the reflection of a wedge-generated oblique shock wave from a symmetry plane in a steady flow, both regular (RR) and irregular (MR) reflections are possible. Ivanov et al [19] describes the flow field as follows: In the regular reflection (Fig 11a), a reflected shock wave (RS) is formed at the intersection point of the incident shock (IS) and the symmetry plane. The flow that passes through the RS returns to its original direction parallel to the symmetry plane. For the irregular (Mach) reflection, the point T where the incident and reflected shocks intersect is located at some distance from the symmetry plane and connected with it by the third shock wave, the Mach stem (MS). (Fig 11b) Besides three shock waves, a slip surface (SS) also comes from the triple point T and divides the streams that passed through the MS and the two shocks, IS and RS. The existence of MR in steady flow is connected with the presence of the length scale (the wedge length,  $w$ ) that controls the MS height,  $H_{st}$ . The trailing edge of a wedge generates an expansion fan that refracts on the RS and then interacts with the SS. Because of this interaction, the slip surface becomes curved and forms “a virtual nozzle”. In this nozzle the flow, turned to subsonic after passing through the MS, accelerates up to a supersonic velocity. Finally, the MS height is defined by the relation between the inlet and throat cross sectional areas of the nozzle.



**Figure 11: Schematic of Mach- and Regular-Reflections of Crossing Oblique Shock Waves.**

The phenomenon of regular and irregular shock reflections has been the subject of numerous investigations [19-24]. For a given Mach number and ratio of specific heats, only regular Reflections (RR) are possible for shock angles where the pressure rise across the primary and secondary oblique shocks is less than the pressure rise across a single normal shock at the freestream Mach number. The condition where the pressure rise across the initial and reflected shocks is equal to the pressure rise across a normal shock at the freestream Mach number is referred to as the Neumann condition. The pressure deflection diagram for the Neumann condition is shown in Fig. 12. The detachment condition is defined as that above which the initial shock wave is too strong for an attached reflected wave. The pressure-deflection diagram for the detachment condition is also shown in Fig. 12. Mach reflections (MR) always result for initial shock angles above the detachment angle. Between the Neumann and detachment conditions lies a range of initial shock angles where both regular and Mach reflections are possible. This region, referred to as the dual reflection domain, is quite small at lower Mach numbers but increases in size to approximately 8.5 degrees for a Mach number of 5. The pressure deflection diagram typical of the dual solution domain is shown in Fig. 12 and the RR, MR and dual solution domains are defined in terms of the initial Mach number and shock angle in Fig. 13.

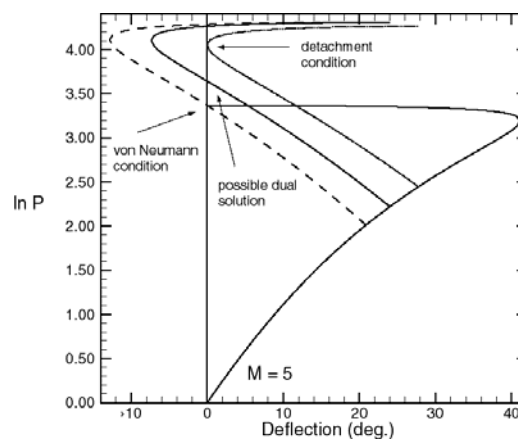


**Figure 12: Pressure-Deflection Diagram Demonstrating the Neumann and Detachment Conditions and the Path for a Possible Dual Solution.**

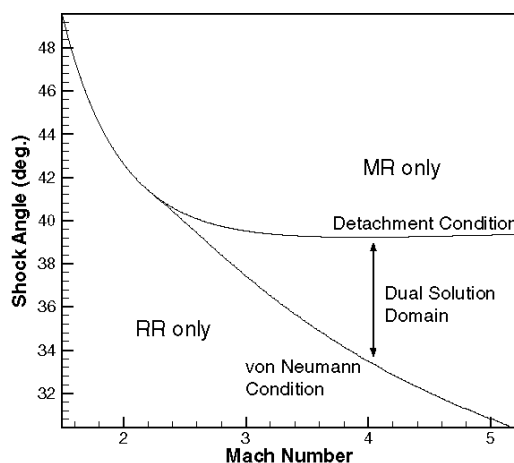


Figure 13: Domains for RR, MR and Possible Dual Solutions.

Historically, much effort has been made to characterize the MR, RR, and dual solution domains. Early analytical and experimental work was done by Henderson [20] and Hornung [24]. Although not seen in early experimental data, Hornung, et al [25], hypothesized the existence of hysteresis for the transition between MR and RR in the dual solution domain. In the hysteresis loop the RR configuration persists for increasing incident shock angles until it transitions to the MR configuration near the detachment condition. Once the MR configuration is established, it persists for decreasing incident shock angles until transitioning back to the RR configuration near the Neumann condition. This hysteresis was later demonstrated in the experiments of Chpoun, et al, [21] and the computations of Vuillon, et al, [22] and Ivanov, et al [19]. Numerical investigations have employed both continuum [19,22] and DSMC approaches [19].

## STEADY SHOCK WAVE REFLECTION TRANSITION AND HYSTERESIS IN TWO DIMENSIONS

### Experimental Data

Experimental data for evaluation of the two-dimensional numerical simulations of crossing oblique shock interactions were collected by the Ivanov group in tunnel T313 at ITAM, Novosibirsk. A schematic of the experimental geometry is shown in Fig. 14. The wedges could be rotated symmetrically about the trailing edges. The freestream Mach number was 5 and the Reynolds number, based on the wedge compression surface length,  $w$ , was 2 million. The wedge aspect ratio was  $b/w = 3.75$ , while the distance between the trailing edge of the wedge and the plane of symmetry was  $g/w = 0.42$ . The theoretical compression and shock angles for the Neumann and detachment conditions are listed in Table 2 where  $\theta$  is the flow deflection angle and  $\alpha$  is the resulting shock-wave angle.

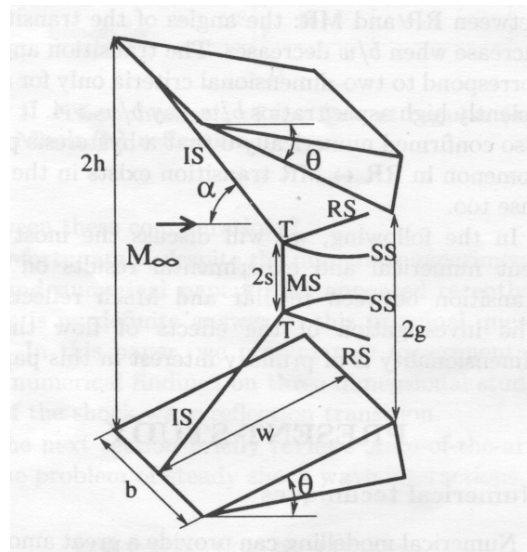


Figure 14: Schematic of the Experimental Configuration used by the Ivanov Group.

Table 2: Theoretical Detachment (D) and Neumann (N) conditions.  
Q is the flow deflection angle and  $\alpha$  is the shock-wave angle

Mach No.	$\theta_D$	$\alpha_D$	$\theta_N$	$\alpha_N$
5	27.7	39.3	20.9	30.9

Laser light-sheet visualization was used to view the shock reflection configuration at constant spanwise distances from the wedge horizontal plan of symmetry. The reflection configuration and Mach-stem height was determined from the light-sheet visualization. A sample image illustrating the technique is shown in Fig. 15.

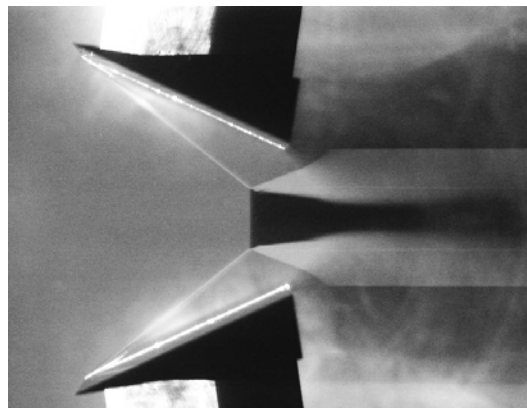


Figure 15: Sample Laser Light-Sheet Visualization from the Ivanov Group.  
 $M = 4$ ,  $\alpha = 37$  degrees,  $b/w = 3.75$ ,  $g/w = 0.3$ .



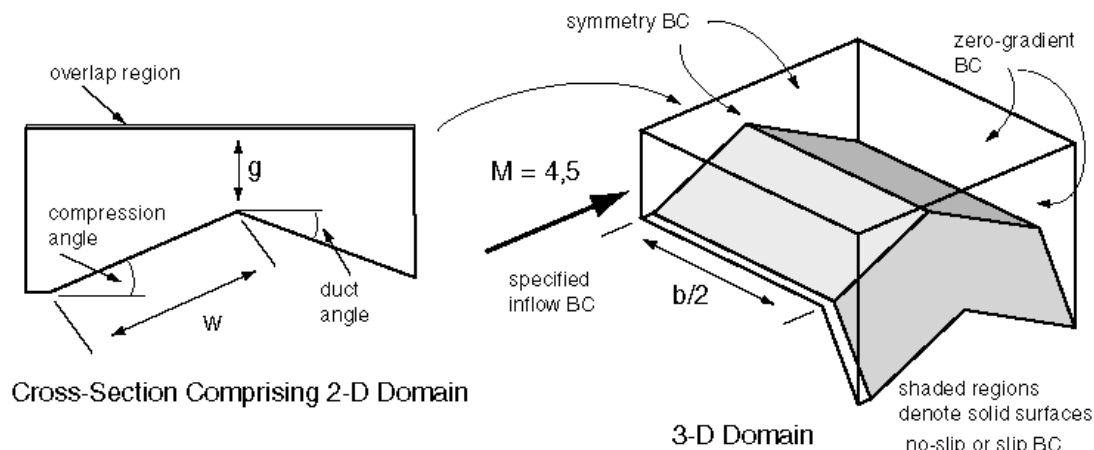


Figure 16: Schematic of the Two- and Three-Dimensional Grids.

## Two-Dimensional Numerical Simulations

Two-dimensional simulations for the geometry and flow conditions defined above were performed by the Ivanov Group at the Institute for Theoretical and Applied Mechanics (ITAM), Novosibirsk, Russia and Schmisser and Gaitonde at the United States Air Force Research Laboratory (AFRL). Both groups used upwind-biased schemes to compute the flows and a common procedure for incorporating changes in the wedge angle. The converged solution at a previous wedge angle was used as the initial condition for the next solution with an incremental change in wedge angle.

The computations of the Ivanov Group were carried out with a multi-block shock capturing Euler TVD code using MUSCL reconstruction of the HLLE (Harten-Lax-van Leer-Einfeldt) solver. Time integration was accomplished with a third-order Runge-Kutta scheme.

In the computations of Schmisser and Gaitonde, two different methods are considered for the discretization of the inviscid components of the governing equations, the Roe scheme [26] and the van Leer scheme [27]. The upwind-biased MUSCL method [27] is used for reconstruction. The viscous fluxes in the governing equations are evaluated with standard second-order central differences. The equations are integrated in time with an implicit approximately-factored scheme [28]. Newton-like subiterations are incorporated to accelerate convergence.

## Grids and Boundary Conditions

The computational domain employed for the two-dimensional simulations of Schmisser and Gaitonde is shown in Fig. 17. Since the geometry is symmetric, only half the physical domain is computed. The upstream boundary is sufficiently forward of the fin leading edges that uniform flow may be specified there. On the solid surfaces the boundary conditions are specified either as slip or no-slip, depending on whether the computations are inviscid or viscous. The downstream boundary condition is set through zero-gradient extrapolation. An overlap region is used to determine the boundary conditions on the symmetry plane. The grid actually extends several points (typically 4 or 8) beyond the symmetry plane in the Y direction, *i.e.*, normal to the incoming flow. The flow conditions in the overlap region are specified to mirror those on the other side of the symmetry plane. The pressure, density and velocity component parallel to the symmetry



plane are set equal to those of their mirror-counterpart mesh points while the velocity normal to the symmetry plane is of equal magnitude but of reversed sign.

The fins end abruptly in the experimental geometry, corresponding to a turning angle typically in excess of 90 degrees. Since the present simulations adopt a continuum approach, it is difficult to simulate such a rapid expansion because of the tendency to obtain unphysically low values of pressure and temperature. To overcome this problem a duct is appended to the end of the compression fins at the trailing edge. Although the nominal duct angle is 25 degrees (with respect to the freestream direction) for the two-dimensional cases, some calculations have explored the impact of the duct angle [18].

Non-uniform but Cartesian grids are employed to discretize the above domain. In several cases the mesh size is varied in order to obtain an estimate of the solution dependence on mesh resolution. Details of the mesh sizes are provided in a later section.

The Euler solutions of the Ivanov group utilize a numerical domain similar to that used by Schmisser and Gaitonde. A notable difference is the expansion used by Schmisser and Gaitonde at the wedge trailing edge is replaced with a horizontal duct in the computations of the Ivanov Group.

### **Demonstration of Hysteresis**

Hysteresis in the shock-reflection configuration for solutions in the dual-solution domain was verified by computing a sequence of solutions with first gradually increasing and then gradually decreasing compression-wedge angles. For a few of the solutions where the wedge angle was gradually increased from an RR solution, uniform flow initial conditions were employed. In terms of the final solution attained, for the demonstration of hysteresis, this approach was similar to that in which the initial condition was a converged RR solution at a lesser wedge angle. (When starting from a uniform flow initial condition the developing shock system propagates away from the fin surface and reflects regularly in the initial transient. See the discussion in Ivanov, et al [19].) All solutions for decreasing fin angles utilized the previous solution for the higher angle as an initial condition to obtain the new solution at the lower angle.

The phenomenon of hysteresis is seen in Fig. 17 which shows the shock structure computed by Schmisser and Gaitonde for two sets of computations with  $g/w = 0.42$  and  $g/w = 0.34$ . The Mach-stem height as a function of the shock wave angle for the cases with  $g/w = 0.34$  is plotted in Fig. 18. In the dual-solution domain, when the initial condition was a regular reflection or uniform flow the RR configuration persisted until the theoretical value of the detachment condition. As may be seen in Fig. 17, for the cases with  $g/w = 0.42$  the transition from RR to MR occurred for a flow deflection angle between 27 and 28 degrees. For the cases with  $g/w = 0.34$  smaller wedge angle increments were employed and the range for transition from RR to MR was narrowed to wedge angles between 27.5 and 27.85 degrees. This range of values is in close agreement with the theoretical value for detachment, 27.7 degrees (see Table 2). For solutions with MR initial conditions the MR pattern persists through much of the dual solution space, but transitions to an RR configuration before the Neumann condition is reached. For the solutions plotted in Fig. 18 the transition from a MR to RR solution occurs for wedge angles between 22 and 23 degrees, a range slightly higher than the theoretical Neumann value of 20.87 degrees.

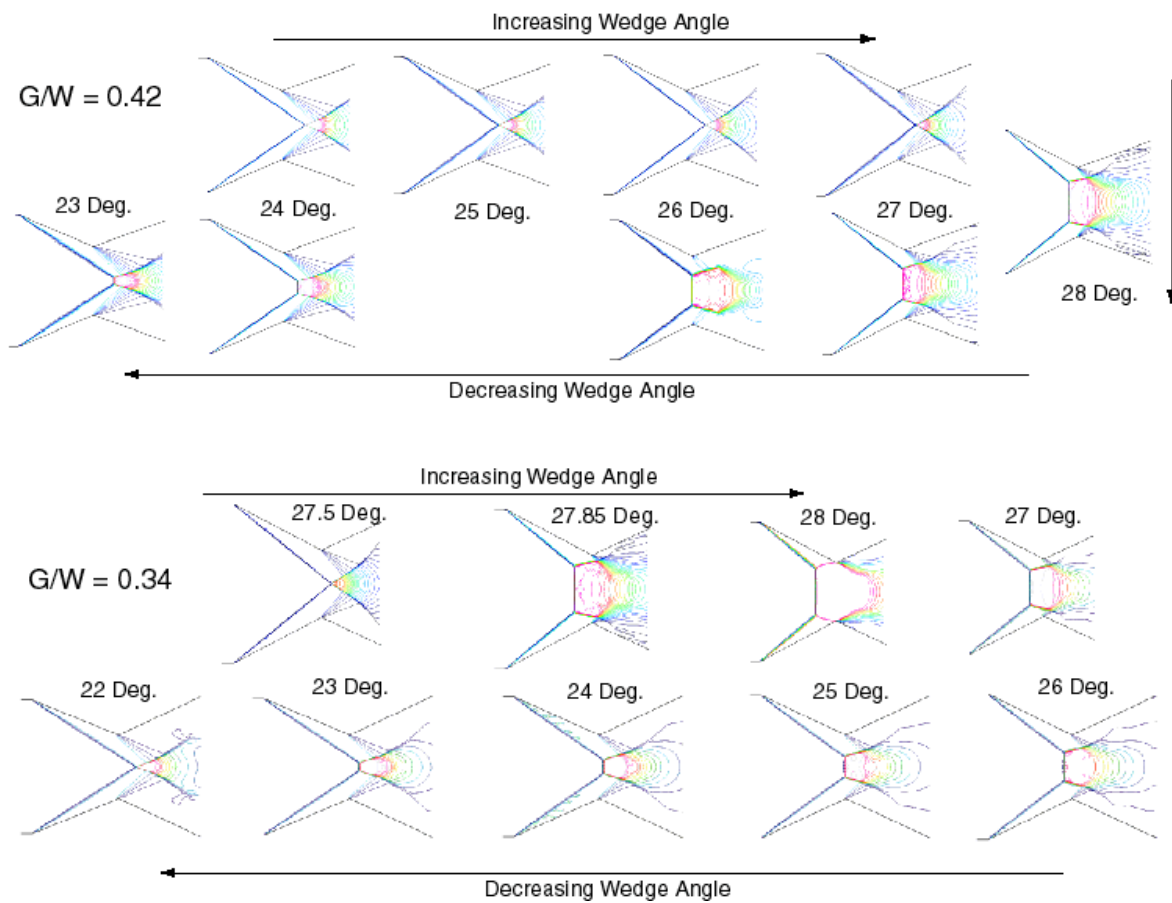


Figure 17: Isobars Demonstrating Hysteresis in 2-D Simulations of Schmisser and Gaitonde.

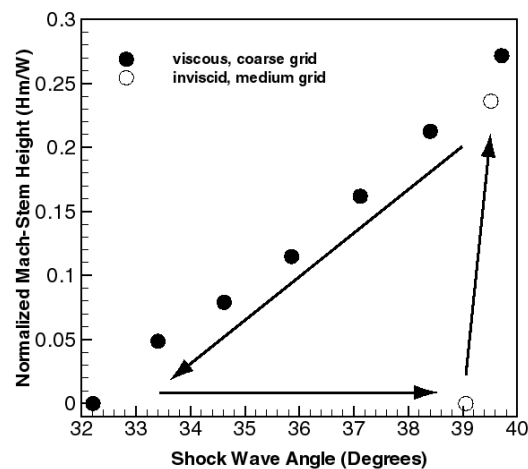
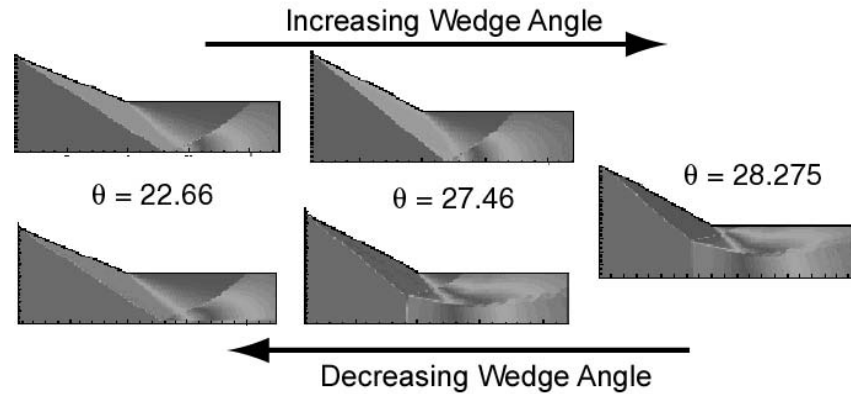


Figure 18: Hysteresis Loop in the Mach-Stem Height as a Function of Wedge Angle for the Cases with  $g/w = 0.34$  (from Schmisser and Gaitonde).

Similar results from the Ivanov Group also demonstrate hysteresis, as shown in Fig. 19. In the figure, five density fields for wedge angles of 22.66, 27.46 and 28.275 degrees are plotted with only one-half of the symmetric flowfield shown. With increasing wedge angle (top row) the regular reflection is maintained until at  $\theta=28.275$  deg. the transition to Mach reflection occurs. With decreasing wedge angle the MR configuration persists, as shown in the bottom row of the figure.



**Figure 19: Density Contours showing Hysteresis in Two-Dimensional Simulations, from the Ivanov Group.**

The hysteresis loop demonstrated by the two-dimensional computations of the Ivanov Group is plotted in Fig. 20. The loop is defined in terms of the computed Mach-stem height (open symbols) and the primary shock wave angle. Dotted lines indicate the theoretical Neumann and detachment conditions while the Mach-stem heights determined from experimental data are shown as the closed symbols. Comparison of Fig. 20 with Fig. 18 reveals that the limiting shock angles in the hysteresis loops determined by both research groups were essentially the same. Transition from RR to MR was observed at the detachment condition while transition from MR to RR occurred at a shock angle slightly higher than the Neumann condition. It has been suggested that the transition from MR to RR at shock angles higher than the Neumann condition results from the limited ability of a reasonably sized computational grid to accurately resolve increasingly smaller Mach-stem heights as the Neumann condition is approached.

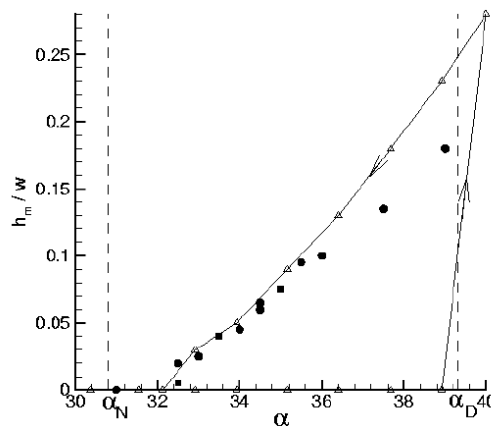


**Figure 20: Numerical and Experimental Mach-Stem Heights as a Function of Primary Shock Angle, from the Ivanov Group.**

In Fig. 21 the Mach-stem heights from the numerical simulations of Schmisser and Gaitonde for  $g/w = 0.34$  are compared with the results of Euler solutions with similar mesh resolution (20,000 to 50,000 nodes) by Ivanov, et al [19] and the experimental data. Generally good agreement is observed between the three data sets. Although the Mach-stem heights determined from the computations of Schmisser and Gaitonde are slightly less than those determined from the computations of Ivanov, et al [19], it is not clear if this is an aspect of the computations or a variation in the definition of the triple-point location used by each group.

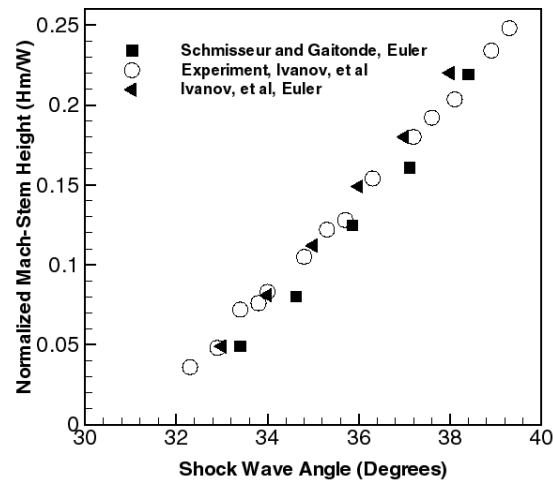


Figure 21: Variation of Mach-Stem Height with Shock Angle for Two-Dimensional Cases.

## STEADY SHOCK WAVE REFLECTION TRANSITION AND HYSTERESIS IN THREE DIMENSIONS

The efforts behind examination of the three-dimensional crossing oblique shock interaction are essentially extensions of those conducted in two dimensions. The participants are the same and both groups employ similar experimental and numerical approaches. One change between the datasets is that the freestream conditions are changed for the three-dimensional efforts. The new freestream Mach number is 4 and the Reynolds number based on the wedge compression surface,  $w$ , is reduced to 1.4 million. Using the laser light-sheet visualization technique described earlier, experimental data for the spanwise variation of Mach-stem height has been provided by the Ivanov Group [29] for the case with  $b/w=3.75$ . The variation in Mach-stem height with primary shock angle on the plane of symmetry is also provided for the cases with  $b/w = 1.0, 2.0, 3.75$ . The Neumann and detachment conditions for the new freestream conditions are listed in Table 3.

Table 3: Theoretical Detachment ( $\theta_D$ ) and Neumann ( $\theta_N$ ) Conditions.  
Q is the flow deflection angle and  $\alpha$  is the shock-wave angle.

Mach No.	$\theta_D$	$\alpha_D$	$\theta_N$	$\alpha_N$
4.0	25.61	39.23	20.86	33.44

The computational domain for the three-dimensional calculations of Schmisser and Gaitonde was shown previously in Fig. 16. For clarity, the solid surfaces are shaded. Both vertical and lateral symmetry are

assumed to reduce computational resource requirements. The mesh is generated by stacking two-dimensional grids in the spanwise direction and within each such plane the boundary conditions are the same as those described above. Constraints similar to those discussed earlier regarding the abrupt trailing edge of the compression fins also apply to the sides of the three-dimensional configurations. Thus, a “spanwise duct” is appended, as shown in the figure, with the duct angle fixed at 60 degrees with respect to the horizontal. Zero-gradient conditions are also applied at the edge of the domain in the spanwise direction.

## Spanwise Variation of Mach-Stem Height

Contours of constant pressure computed by Schmisser and Gaitonde for planes of constant spanwise distance from the centerline are plotted in Fig. 22 for the interaction generated by 23.9 deg. compression fins. The spanwise distance from the centerline is noted next to each subplot. A clear MR configuration is clearly seen in all the spanwise sections. At the centerline,  $z/w=0$ , the Mach-stem occupies a significant portion of the area between the compression surfaces and occurs upstream of the throat. At large spanwise distances from the centerplane, the Mach-stem decreases in size and occurs at locations further downstream. While the first evidence of this in the limited number of slices shown in Fig. 22 is seen in the plot for  $z/w = 1.242$ , the phenomenon is prominent in the contours for  $z/w = 1.721$ . The Mach-stem occurs at the streamwise location of the throat at  $z/w = 1.800$ . At the spanwise limit of the wedge face,  $z/w=1.875$ , the Mach-stem occurs slightly downstream of the throat.

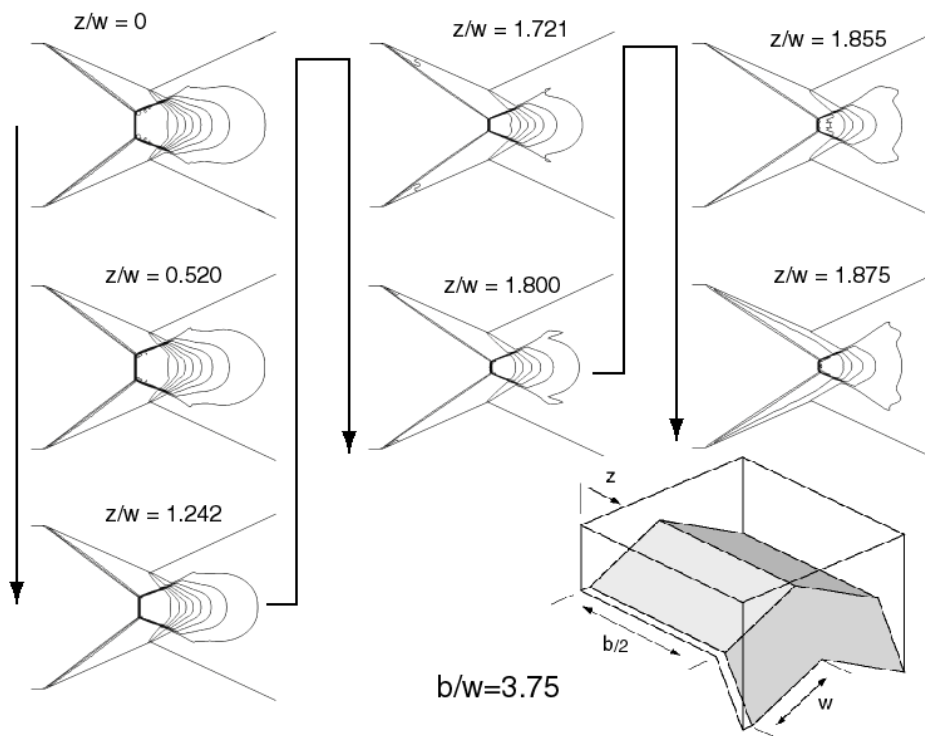


**Figure 22: Variation of Shock Wave Structure with Spanwise Location for 23.9 deg. Wedge Angle,  $b/w=3.75$ .**

The spanwise variation of computed Mach stem height for the simulations of both Schmisser and Gaitonde and the Ivanov Group is compared with the experimental data of Ivanov, et al, [29] in Fig. 23. For the simulations of Schmisser and Gaitonde the uncertainty in the Mach-stem height is of the size of the mesh spacing. Both sets of numerical simulations closely predict the spanwise variation in Mach-stem height exhibited by the experimental data. The height of the Mach stem decreases from a maximum value at the center plane ( $z/w = 0$ ) to a minimum value at the edge of the compression surface ( $z/w = 1.875$ ) and subsequently in the spanwise expansion region ( $z/w > 1.875$ ) the Mach-stem height increases again. This increase in Mach-stem height, in the region beyond the spanwise limit of the compression surface, is accompanied by downstream movement of this feature. Indeed, the spanwise relief effect weakens the primary shock to yield the situation where the flow downstream of the Mach-stem is supersonic and is accompanied by a significant spanwise velocity. The phenomenon in this region is sometimes referred to as a peripheral Mach reflection.

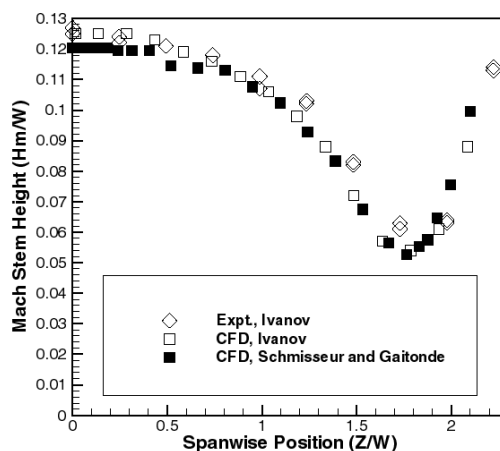


**Figure 23: Spanwise Variation of Mach-Stem Height for  $b/w=3.75$ , Mach 4, 23.8 deg. Flow Deflection Angle (37 deg. shock angle),  $g/w=0.3$ . Experimental data from Ivanov, et al.**

## Variation of Mach-Stem Height with Shock Angle

The Mach-stem height on the symmetry plane is plotted against the shock wave angle in Figs.24-25 for the three-dimensional simulations and experimental data [29] of the Ivanov Group for  $b/w = 2.0$  and  $3.75$ . The data in both figures exhibit generally close agreement between the measured and numerically simulated Mach-stem heights.

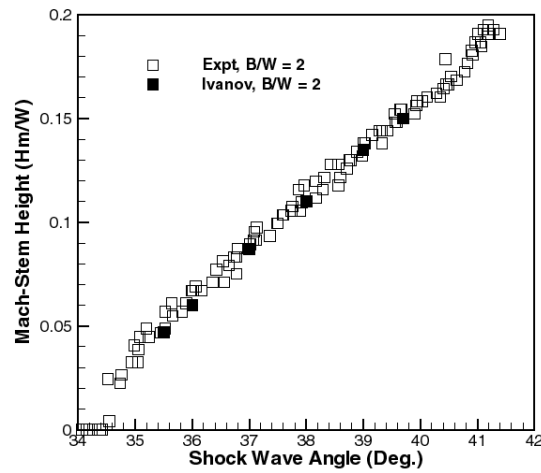


Figure 24: Variation of Mach-Stem Height with Shock Angle for  $b/w = 2.0$ .

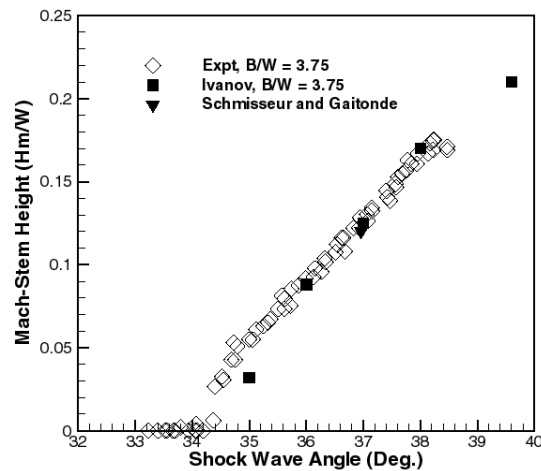


Figure 25: Variation of Mach-Stem Height with Shock Angle for  $b/w=3.75$ .

## CONCLUSIONS

As part of an effort to advance technologies related to hypersonic flight the NATO RTO WG10 has examined the current capability of numerical simulations to predict laminar shock-shock interactions. Two geometrically simple, yet computationally challenging, flow fields were investigated: the Edney IV and oblique crossing shock interactions. The following conclusions may be drawn from analysis of the experimental and computational contributions to this effort.

### **Edney IV Interaction**

The capabilities of both Navier-Stokes and DSMC solutions to predict Edney IV interactions were considered. Based on the simulations examined in this study, no clear advantage was observed in choosing one technique over the other. While both numerical approaches captured the general trends observed in the measured data, both techniques tended to overestimate the measured peak pressure and heat transfer in the interaction. Questions remain regarding whether this overestimation of measured quantities is a result of deficiencies in the numerical model or inadequate resolution and unsteadiness in the experiments (or some combination of both).

Upon initial review, the inability of the simulations to accurately predict the location of the peak measured quantities without prior knowledge of the experimental results might cause concern. However, when the extreme sensitivity of the interaction to the precise intersection point of the incident and bow shocks and the possibility of subtle freestream nonuniformities in ground test facilities is considered, the inability to predict the peak locations *a priori* should not be considered a defect in the numerical approach.

### **Oblique Crossing Shock Interaction**

Oblique crossing shock interactions in steady flows with conditions in the dual-solution domain were examined both numerically and experimentally. Two- and three-dimensional simulations were compared with the measured Mach-stem heights determined from flow visualization.

Hysteresis in the shock-reflection configuration was demonstrated for two-dimensional solutions with the same limits of the hysteresis loop observed by both participating research groups. The transition from regular to Mach reflection occurs very near the theoretical detachment condition, while for decreasing flow deflection angles the transition from Mach to regular reflection occurs before the flow deflection angle has decreased to the Neumann condition. Both the two- and three-dimensional solutions show reasonable agreement between the numerical and experimental Mach-stem heights on the interaction centerline. Additionally, the three-dimensional simulations closely predict the spanwise variation of the Mach-stem height observed in the experiments.

While numerical simulations of the oblique crossing shock interaction appear to predict the shock structure with reasonable accuracy, the question of which reflection configuration (Mach or regular) is correct for flows in the dual-solution domain remains an issue. Computations of these interactions accurately predict the resulting flow as long as the correct initial conditions (either Mach or regular reflection) are employed. Outstanding questions remain regarding which configuration should be expected in real flows within the dual-solution domain and what initial conditions should be employed to ensure prediction of the same shock structure observed in real flows.

### **ACKNOWLEDGMENTS**

The authors are grateful for the enthusiastic efforts of all the participants in the validation study. Special thanks go to Dr. Mike Holden of CUBRC whose energy and vision ignited the authors' interest in the area of CFD validation. Portions of the work reported in this manuscript were supported by the Air Force Office of Scientific Research and the DoD HPC Shared Resource Centers.



## REFERENCES

- [1] B. Edney, Anomalous heat transfer and pressure distributions on blunt bodies at hypersonic speeds in the presence of an impinging shock. Rep. 115, Flygtekniska Forsöksanstalten (The Aeronautical Research Institute of Sweden), Stockholm, 1968.
- [2] H. Hornung, Regular and Mach reflection of shock waves. *Annual Review of Fluid Mechanics*, 18:33-58, 1986.
- [3] Watts J.D., Flight experience with shock impingement and interference heating on the X-15-2 research airplane, NASA TM X-1669, 1968.
- [4] Holden M.S., Moselle J.R., Lee J., Weiting A.R., and Glass C., Studies of aerothermal loads generated in regions of shock-shock interaction in hypersonic flow, NAS1-17721, 1991.
- [5] Carlsen A.B. and Wilmoth R.G., Monte Carlo simulation of a near-continuum shock-shock interaction problem, AIAA 27<sup>th</sup> Thermophysics Conference, Nashville, TN, 1992.
- [6] Pot T, Chanetz B, Lefebvre M, Bouchardy P., Fundamental study of shock/shock interference in low density flow. Presented at the 21<sup>st</sup> International Symposium on Rarefied Gas Dynamics, 1998.
- [7] Bird G.A., The G2/A3 program users manual. G.A.B. Consulting Pty Ltd, Killara, N.S.W., Australia, 1992.
- [8] Moss J.N., Pot T., Chanetz B., and Lefebvre M. (1999), DSMC simulation of shock/shock interactions: Emphasis on type IV interactions. Paper No. 3570, 22<sup>nd</sup> International Symposium on Shock Waves (Issw22), Imperial College, London, UK, 1999.
- [9] Holden M.S., A review of the aerothermal characteristics of laminar, transitional, and turbulent shock-shock interaction regions in hypersonic flows, AIAA 98-0899, 1998.
- [10] Holden M.S., Database of aerothermal measurements in hypersonic flow for CFD validation, CUBDAT Version 2.2 CDROM, Calspan-University of Buffalo Research Center, 1999.
- [11] MacCormack, R.W. and G.V. Candler, The solution of the Navier-Stokes equations using Gauss-Seidel line relaxation, *Computers and Fluids*, Vol. 17, No. 1, pp. 135-150, 1989.
- [12] Candler, G.V. and R.W. MacCormack, The computation of hypersonic ionized flows in chemical and thermal nonequilibrium, *Journal of Thermophysics and Heat Transfer*, Vol. 5, No. 3, pp. 266-273, 1991.
- [13] Wright, M.J., D. Bose, and G.V. Candler, A data-parallel line relaxation method for the Navier-Stokes equations, *AIAA Journal*, Vol. 36, No. 9, pp. 1603-1609, 1998.
- [14] Dietrich, S. and Boyd, I. D., Scalar optimized parallel implementation of the direct simulation Monte Carlo method, *Journal of Computational Physics*, Vol. 126, pp. 328-342, 1996.
- [15] Koura, K. and Matsumoto, H., Variable soft sphere molecular model for air species, *Physics of Fluids A*, Vol. 4, pp. 1083-1085, 1992.

- [16] Boyd, I. D., Analysis of rotational nonequilibrium in standing shock waves of Nitrogen, *AIAA Journal*, Vol. 28, pp. 1997-1999, 1990.
- [17] Vijayakumar, P., Sun, Q. and Boyd, I. D., Detailed models of vibrational-translational energy exchange for the direct simulation Monte Carlo method, *Physics of Fluids*, Vol. 11, pp. 2117-2126, 1999.
- [18] Schmisser J.D. and Gaitonde D.V., Numerical simulation of Mach reflection in steady flows, AIAA 2001-0741, 2001.
- [19] Ivanov M.S., Markelov G.N., Kudryavtsev A.N., and Gimelshein S.F., Numerical analysis of shock wave reflection transition in steady flows, *AIAA Journal*, Vol. 36, No. 11, 1998.
- [20] Henderson, L.F. The reflexion of a shock wave at a rigid wall in the presence of a boundary layer. *Journal of Fluid Mechanics*, 30:699-722, 1967.
- [21] A. Chpoun, D. Passerel, H. Li, and G. Ben-Dor. Reconsideration of oblique shock wave reflections in steady flows. part 1. experimental investigation. *Journal of Fluid Mechanics*, 301:19--35, 1995.
- [22] J. Vuillon, D. Zeitoun, and G. Ben-Dor. Reconsideration of oblique shock wave reflections in steady flows. part 2. numerical investigation. *Journal of Fluid Mechanics*, 301:37--50, 1995.
- [23] H. Li and G. Ben-Dor. A parametric study of Mach reflection in steady flows. *Journal of Fluid Mechanics*, 341:101-125, 1997.
- [24] H. Hornung and M. Robinson. Transition from regular to Mach reflection of shock waves part 2. the steady-flow criterion. *Journal of Fluid Mechanics*, 123:155-164, 1982.
- [25] H. Hornung, H. Oertel and R. Sandeman. Transition from Mach reflection of shock waves in steady and pseudosteady flow with and without relaxation. *Journal of Fluid Mechanics*, 90:541-560, 1979.
- [26] P. Roe. Approximate Riemann Solvers, Parameter Vectors and Difference Schemes. *Journal of Computational Physics*, 43:357--372, 1981.
- [27] B. van Leer. Flux-Vector Splitting for the Euler Equations. *Lecture Notes in Physics*, 170:507--512, 1982.
- [28] R. Beam and R. Warming. An implicit factored scheme for the compressible Navier-Stokes Equations. *AIAA Journal*, 16(4):393-402, 1978.
- [29] M. Ivanov, A. Kharitonov, D. Khotyanovsky, A. Kudryavtsev, G. Markelov, and S. Nikiforov. Numerical and experimental study of 3 -D steady shock wave interactions. Paper 2001-0740, AIAA 39th Aerospace Sciences Meeting, Reno, NV, January 2001.

***This paper is a work of the U.S. Government and is not  
subject to copyright protection in the United States.***

